



XO-7 b: A Transiting Hot Jupiter with a Massive Companion on a Wide Orbit

Nicolas Crouzet¹, Brian F. Healy², Guillaume Hébrard³, P. R. McCullough^{2,4}, Doug Long⁴, Pilar Montañés-Rodríguez^{5,6}, Ignasi Ribas^{7,8}, Francesc Vilardell^{7,8}, Enrique Herrero^{7,8}, Enrique García-Melendo^{9,18}, Matthieu Conjat¹⁰, Jerry Foote¹¹, Joe Garlitz¹², Phillip Vo¹³, Nuno C. Santos^{14,15}, Jos de Bruijne¹, Hugh P. Osborn¹⁶, Shweta Dalal³, and Louise D. Nielsen¹⁷

¹ Science Support Office, Directorate of Science, European Space Research and Technology Centre (ESA/ESTEC), Keplerlaan 1, 2201 AZ Noordwijk, The Netherlands; nicolas.crouzet@esa.int

² Department of Physics and Astronomy, Johns Hopkins University, 3400 North Charles Street, Baltimore, MD 21218, USA

³ Institut d'Astrophysique de Paris, UMR7095 CNRS, Université Pierre & Marie Curie, 98bis boulevard Arago, F-75014 Paris, France

⁴ Space Telescope Science Institute, 3700 San Martin Drive, Baltimore, MD 21218, USA

⁵ Instituto de Astrofísica de Canarias, C. Vía Láctea s/n, E-38205 La Laguna, Tenerife, Spain

⁶ Universidad de La Laguna, Dept. de Astrofísica, E-38206 La Laguna, Tenerife, Spain

⁷ Institut de Ciències de l'Espai (CSIC-IEEC), Campus UAB, Carrer de Can Magrans s/n, E-08193 Bellaterra, Spain

⁸ Institut d'Estudis Espacials de Catalunya (IEEC), Gran Capità, 2-4, Edif. Nexus, E-08034 Barcelona, Spain

⁹ Escola Superior d'Enginyeries Industrial, Aeroespacial i Audiovisual, Universitat Politècnica de Catalunya, Carrer Colom 1, E-08222 Terrassa, Spain

¹⁰ Observatoire de la Côte d'Azur, Boulevard de l'Observatoire, CS 34229, F-06304 Nice Cedex 4, France

¹¹ Vermillion Cliffs Observatory, 4175 E. Red Cliffs Drive, Kanab, UT 84741, USA

¹² Elgin Observatory, Elgin, OR, USA

¹³ Department of Physics and Astronomy, University of Waterloo, Waterloo, ON, N2L 3G1, Canada

¹⁴ Instituto de Astrofísica e Ciências do Espaço, Universidade do Porto, CAUP, Rua das Estrelas, 4150-762 Porto, Portugal

¹⁵ Departamento de Física e Astronomia, Faculdade de Ciências, Universidade do Porto, Rua do Campo Alegre, 4169-007 Porto, Portugal

¹⁶ Aix Marseille Université, CNRS, CNES, LAM (Laboratoire d'Astrophysique de Marseille), F-13388 Marseille, France

¹⁷ Observatoire de Genève, Université de Genève, 51 Chemin des Maillettes, 1290 Sauverny, Switzerland

Received 2019 August 6; revised 2019 November 20; accepted 2019 November 23; published 2020 January 10

Abstract

Transiting planets orbiting bright stars are the most favorable targets for follow-up and characterization. We report the discovery of the transiting hot Jupiter XO-7 b and of a second, massive companion on a wide orbit around a circumpolar, bright, and metal-rich G0 dwarf ($V = 10.52$, $T_{\text{eff}} = 6250 \pm 100$ K, $[\text{Fe}/\text{H}] = 0.432 \pm 0.057$ dex). We conducted photometric and radial velocity follow-up with a team of amateur and professional astronomers. XO-7 b has a period of 2.8641424 ± 0.0000043 days, a mass of $0.709 \pm 0.034 M_J$, a radius of $1.373 \pm 0.026 R_J$, a density of $0.340 \pm 0.027 \text{ g cm}^{-3}$, and an equilibrium temperature of 1743 ± 23 K. Its large atmospheric scale height and the brightness of the host star make it well suited to atmospheric characterization. The wide-orbit companion is detected as a linear trend in radial velocities with an amplitude of $\sim 100 \text{ m s}^{-1}$ over two years, yielding a minimum mass of $4 M_J$; it could be a planet, a brown dwarf, or a low-mass star. The hot Jupiter orbital parameters and the presence of the wide-orbit companion point toward a high-eccentricity migration for the hot Jupiter. Overall, this system will be valuable to understand the atmospheric properties and migration mechanisms of hot Jupiters and will help constrain the formation and evolution models of gas giant exoplanets.

Unified Astronomy Thesaurus concepts: Exoplanet astronomy (486); Exoplanets (498); Extrasolar gas giants (509); Hot Jupiters (753); Transits (1711); Transit photometry (1709); Transit instruments (1708); Exoplanet systems (484); High-resolution spectroscopy (2096); Surveys (1671); Visible astronomy (1776); Radial velocity (1332)

1. Introduction

Gas giant planets transiting bright stars on a close-in orbit are favorable targets for detailed studies. They can be detected and followed-up in photometry and radial velocity (RV), and their atmosphere can be observed by spectroscopy. Ground-based surveys with small apertures and wide fields of view such as WASP (Pollacco et al. 2006; Collier Cameron et al. 2007), HATNet (Bakos et al. 2004), HATSouth (Bakos et al. 2013), KELT (Pepper et al. 2007), and QES (Alsubai et al. 2013) discovered most of the hot Jupiters known to date including ~ 90 around relatively bright stars ($V < 11$). The *CoRoT* (Baglin et al. 2009) and *Kepler* (Borucki et al. 2010) missions detected a few such systems but they targeted mostly fainter stars. The *TESS* mission (Ricker et al. 2015) is an all sky survey and should detect nearly all hot Jupiters transiting stars of magnitude $I < 13$ (Sullivan et al. 2015, 2017).

The presence of wide-orbit companions in hot Jupiter systems draws particular interest. Two mechanisms have been proposed to bring gas giant planets to close-in orbits: disk migration or high-eccentricity migration. The latter requires a high initial eccentricity, potentially due to scattering by another massive companion. These migration mechanisms should, in principle, be reflected in the orbital parameters of hot Jupiters (Faber et al. 2005). In addition, wide-orbit companions may affect the orbit of planets that are closer to the star in the form of an exchange between eccentricity and inclination via the Lidov–Kozai mechanism (Kozai 1962; Lidov 1962). This mechanism has been investigated to explain the eccentricity and obliquity distributions of hot Jupiters. However, no correlation has been found between misaligned or eccentric hot Jupiters and the frequency of massive companions on wide orbits (Knutson et al. 2014; Ngo et al. 2015, 2016; Piskorz et al. 2015). In their sample of 51 planets, Knutson et al. (2014) find statistically significant accelerations in 15 systems and derive an occurrence rate of $51\% \pm 10\%$ for companions with masses between 1 and $13 M_J$ and orbital semimajor axes

¹⁸ Serra Hünter Fellow.

between 1 and 20 au. To date, 10 systems with a transiting hot Jupiter and a massive, well characterized, wide-orbit planetary companion are known (HAT-P-13, HAT-P-17, HAT-P-44, HAT-P-46, HATS-59, HD 219134, KELT-6, WASP-41, WASP-47, WASP-134).¹⁹ Discovering and characterizing such systems will help shed light on the formation and orbital evolution of gas giant exoplanets.

The XO project (McCullough et al. 2005) is targeted at detecting transiting exoplanets around bright stars from the ground with small telescopes. The project started in 2005 and discovered five close-in gas giant planets, XO-1b to XO-5b (McCullough et al. 2006, 2008; Burke et al. 2007, 2008; Johns-Krull et al. 2008). A second version of XO was deployed in 2011 and 2012 and operated from 2012 to 2014. This led to the discovery of XO-6 b, a hot Jupiter transiting a fast-rotating F5 star on an oblique orbit (Crouzet et al. 2017). In this paper, we report the discovery of XO-7 b, a transiting hot Jupiter orbiting a bright G0V star with a massive companion on a wide orbit. We present the instrumental setup and data reduction used to detect the transiting object in Section 2, and describe the follow-up campaign by amateur and professional astronomers to characterize the system in Section 3. The analysis of these data is detailed in Section 4. The XO-7 system properties are given in Section 5 and discussed in Section 6. Conclusions are given in Section 7.

2. XO Photometry

The second version of XO consists of three identical units located at Vermillion Cliffs Observatory, Kanab, Utah, at Observatorio del Teide, Tenerife, Canary Islands, and at Observatori Astronòmic del Montsec (OAdM), Sant Esteve de la Sarga, Spain. Each unit is composed of two 10 cm diameter and 200 mm focal length Canon telephoto lenses equipped with an Apogee E6 1024 × 1024 pixels CCD camera and an *R* band filter, mounted on a German-Equatorial Paramount ME mount and protected by a shelter with a computer-controlled roof. Each unit operates robotically. The six lenses and cameras operate in a network configuration and point toward the same fields of view, which do not overlap with those of the original XO survey. The CCDs are used in Time Delayed Integration (TDI): pixels are read continuously while stars move along columns on the detector. The recorded images are long strips of $43.2^\circ \times 7.2^\circ$. This technique maximizes the number of observed bright stars and increases the observing efficiency. The exposure time is 5.3 minutes for a full strip and the nominal point-spread function FWHM is 1.2 pixels. We observed two strips starting from the north celestial pole and descending along R.A. 6^h and 18^h over two separate nine-month periods between 2012 and 2014.

We carved the strips into 1024×1024 pixel images, which yields 9 fields of $7.2^\circ \times 7.2^\circ$ with a pixel scale of $25.3'' \text{ pixel}^{-1}$. We performed the astrometry using the *astrometry.net* software program²⁰ (Lang et al. 2010) followed by a six-parameter astrometric solution. Science frames are calibrated with darks and flat fields, which are one-dimensional arrays for TDI images, and corrected for warm columns. We ran circular aperture photometry using the Stellar Photometry Software program (Janes & Heasley 1993) with an aperture size optimized as a function of stellar magnitude. We implemented several photometric calibrations and

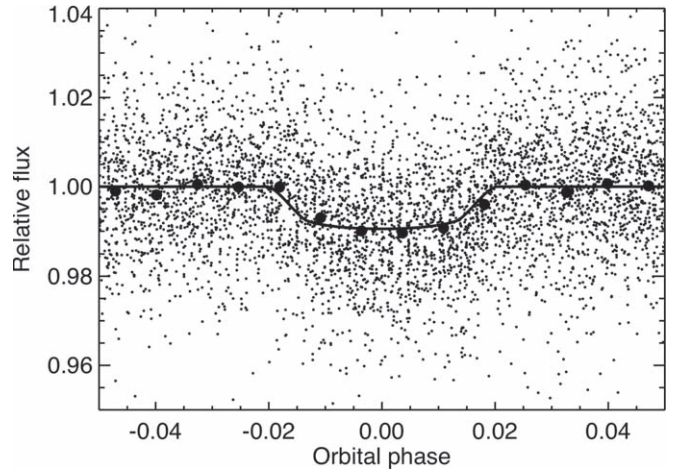


Figure 1. Phase-folded discovery lightcurve of XO-7 b showing the original data (black dots), the data binned over 30-minute intervals (black filled circles), and the best transit fit using the parameters from Table 3 (black line).

built light curves for the 2000 brightest stars in each square field of view (up to $V = 12$). We removed systematic effects using the SYSREM algorithm (Tamuz et al. 2005), combined the light-curves from the six cameras, searched for periodic signals using the Box Least Square algorithm (Kovács et al. 2002), and kept the signals that were compatible with planetary transits for visual inspection. More details on the instrumental setup, instrumental performances, and data reduction procedure can be found in McCullough et al. (2005), Crouzet et al. (2017), and Crouzet (2018).

The phase-folded discovery lightcurve of XO-7 b is shown in Figure 1. The host star is relatively bright (BD+85 317, $V = 10.52$, see Table 2). We gathered 43,880 exposures of this object between 2012 September 28 and 2014 June 7. The light curve dispersion calculated using an outlier-resistant estimate over the out-of-transit data points is 1.1%. After binning the light curve over a timescale of 30 minutes, the dispersion is 0.6%. After phasing the light curve at the planet’s orbital period and binning over 30 minutes (137 phase bins), the dispersion drops to 0.09% (900 ppm) owing to the large quantity of collected data. The transit seen in the discovery light curve motivated an extensive follow-up campaign to characterize this system.

3. Follow-up Campaign

3.1. Faint Nearby Star

The planet host star has a nearby star at a separation of $8''$ that is five magnitudes fainter ($G = 15.8407$, where G is the *Gaia* G band magnitude). This neighbor is a K star ($T_{\text{eff}} = 4038 \text{ K}$, $BP - RP = 1.87$, where BP and RP are magnitudes from the *Gaia* blue and red photometers), it has a parallax of $2.9315 \pm 0.0354 \text{ mas}$, a proper motion of 0.947 ± 0.066 and $17.027 \pm 0.082 \text{ mas yr}^{-1}$ in R.A. and decl., respectively, and an estimated distance of $338 \pm 4 \text{ pc}$ as inferred from *Gaia* DR2 (Bailer-Jones et al. 2018; *Gaia* Collaboration et al. 2018). It is located about 140 pixels in the scan direction on the *Gaia* detectors and does not affect the astrometry of the main target (which could be the case for separations of 10–20 pixels). Its *Gaia* DR2 astrometric data do not show anything suspicious. The parallax, proper motion, and distance of the main target are reported in Table 2. These measurements show that both stars are unbound and the K star is

¹⁹ Source: <http://exoplanet.eu/>.

²⁰ <http://astrometry.net/>

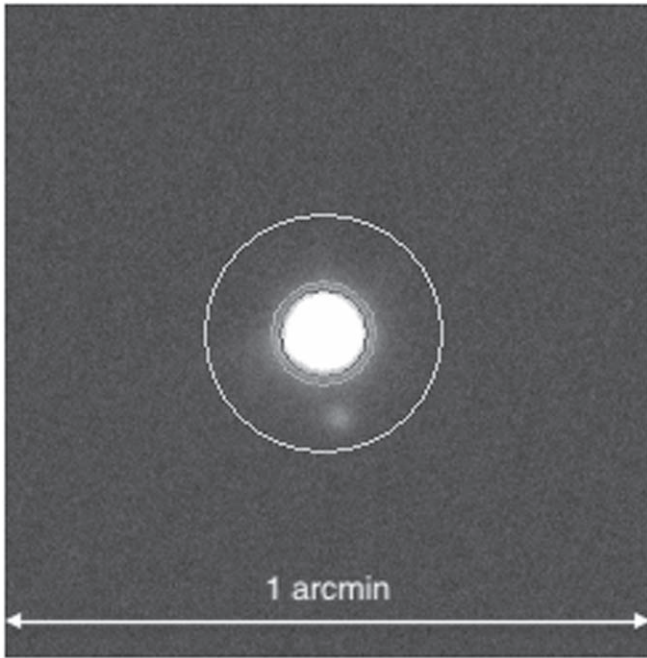


Figure 2. Example of an image cropped around the planet host star XO-7 (BD +85 317) taken during the photometric follow-up with the 40 cm Schaumasse telescope at the Observatoire de Nice, France. The background K dwarf is located $8''$ away from the planet host star and is well resolved. The circular aperture and the annulus used to measure the stellar flux and the sky background respectively are shown.

in the background. They are not resolved by the XO instruments but the K star is faint enough to be negligible at the level of precision of the XO data. Both stars are well resolved in the follow-up observations (Figure 2). No other companion with a magnitude difference less than five is present within 1 arcmin in the bands used for the detection and follow-up (from B to i').

3.2. Photometric Follow-up

Extensive photometric follow-up was conducted by a team of amateur and professional astronomers. We observed 22 transit events between 2017 June 12 and 2018 December 14 with facilities reported in Table 1 using different filters (B , V , g' , R , r' , i') or without a filter (labeled C for “Clear”). We obtained 32 good-quality light curves that we used in the analysis (Figures 3 and 4).

Observations with the 40 cm Schaumasse telescope at the Observatoire de Nice (Nice, France) were conducted using a Johnson B or R filter, sometimes alternating between the two. The images were calibrated using bias, darks, and flat fields. We reduced the data with the IRIS astronomical image processing software (Buil 2005) and performed differential aperture photometry with four reference stars chosen from their brightness and photometric stability. Observations with the 80 cm Telescopi Joan Oró telescope at Montsec Astronomical Observatory (Lleida, Spain) were conducted with the MEIA2 instrument, a $2k \times 2k$ Andor CCD camera with a pixel scale of $0''.36$ and a squared field of view of $12'/3$, using a Johnson V filter. The images were calibrated with darks, bias, and flat fields with the ICAT pipeline (Colome & Ribas 2006). Differential photometry was extracted with AstroImageJ (Collins et al. 2017) using the aperture size and the set of comparison stars that minimized the rms of the out-of-transit photometry. Observations with the 30 cm telescope at Elgin

Observatory (Elgin, Oregon, USA) were conducted using a CCD without a filter. The images were calibrated using bias, darks, and flat fields. We reduced the data with the AIP4Win v2.4.8 Magnitude Measurement Tool (Berry & Burnell 2005) and performed differential aperture photometry with three or five reference stars depending on the image and seeing quality. These stars were selected for each data set based on lowest noise and lack of curvature in the lightcurve and were averaged. Observations with the 40 cm telescopes of the Las Cumbres Observatory Global Telescope network (LCOGT) were conducted using Sloan Digital Sky Survey (SDSS) g' , r' , and i' filters. The images were reduced with the LCOGT’s BANZAI pipeline (McCully et al. 2018) including bad-pixel masking, bias and dark subtraction, flat-fielding, and image plate solving from astrometry.net (Lang et al. 2010). We performed aperture photometry using the Astropy Photutils package (Bradley et al. 2019). Changes in the target star’s position on the detector between nights led us to use nine reference stars for the g' band and 10 for the r' and i' bands.

We gathered these light curves using a consistent format and analyzed them jointly. We converted the dates into Barycentric Julian Date (BJD) and performed a transit fit for each bandpass, during which each light curve was corrected for a linear trend and outliers more than three sigma away were removed. We used these consistent, corrected light curves for the combined fit in Section 4.2.

3.3. RV Follow-up

RV measurements were obtained between 2016 July 23 and 2018 July 4 with the SOPHIE spectrograph (Perruchot et al. 2008; Bouchy et al. 2009, 2013) at the 193 cm telescope of Observatoire de Haute-Provence, France (Figure 5, Appendix). We used its High-Resolution mode (resolving power $R = 75,000$). Exposure times were around 13 minutes allowing signal-to-noise ratios of around 27 per pixel at 550 nm to be reached on most of the exposures. We used the SOPHIE pipeline to extract the spectra from the detector images, cross-correlate them with a numerical mask to produce clear cross-correlation functions (CCFs), then fit the CCFs by Gaussian curves to derive the RVs (Baranne et al. 1996; Pepe et al. 2002).

The resulting CCFs have a contrast that represents $\sim 31\%$ of the continuum, and a FWHM of 11.0 km s^{-1} showing some stellar rotation (we measured $v \sin i = 6 \pm 1 \text{ km s}^{-1}$ from the CCF width; see Section 4.1). The RVs have typical uncertainties around $\pm 13 \text{ m s}^{-1}$, whereas we removed from our final data set three exposures having uncertainties larger than $\pm 30 \text{ m s}^{-1}$. Only five spectra were contaminated by moonlight. We estimated and corrected for that contamination by using the second SOPHIE fiber aperture, which was placed on the sky while the first aperture pointed toward the target (e.g., Hébrard et al. 2008; Bonomo et al. 2010); this resulted in RV corrections around 35 m s^{-1} or smaller (whereas the dispersion of the residuals after the combined fit in Section 4.2 is 14.7 m s^{-1}). Excluding those five Moon-contaminated observations does not significantly change our results. The final RV data set shows significant variations in phase with the transit ephemeris and with a semi-amplitude around 80 m s^{-1} implying a companion mass in the giant-planet regime, as shown in Figure 5.

Radial velocities measured using different stellar masks (G2, K0, or K5) produce variations with similar amplitudes, so it is unlikely that these variations are produced by blend scenarios composed of stars of different spectral types. We finally adopted the RVs obtained with the K0 mask as they provide the

Table 1
Facilities used for the Photometric Follow-up

Observatory	Telescope	Label
Observatoire de Nice, France (a) 2017 Jun 12, (b) 2017 Jul 2, (c) 2017 Jul 25, (d) 2017 Aug 14 (e) 2017 Aug 17, (f) 2017 Sep 6, (g) 2018 Aug 7, (h) 2018 Aug 27	Schaumasse, 16 inches (40 cm) FOV: $31' \times 23'$; Pixel size: $0''.56 \text{ px}^{-1}$	NICE
Observatori Astronòmic del Montsec, Catalonia, Spain (a) 2017 Jun 12, (b) 2017 Jul 2, (c) 2017 Sep 6, (d) 2017 Oct 14 (e) 2017 Oct 16, (f) 2017 Nov 26, (g) 2018 Aug 5, (h) 2018 Aug 7 (i) 2018 Dec 14	Joan Oró Telescope, 31 inches (80 cm) FOV: $12\frac{1}{3} \times 12\frac{1}{3}$; Pixel size: $0''.36 \text{ px}^{-1}$	TJO
Elgin Observatory, Elgin, Oregon, USA (a) 2017 Jun 24, (b) 2017 Jul 17, (c) 2017 Aug 6, (d) 2017 Aug 9	12 inches (30 cm) FOV: $15\frac{1}{7} \times 10\frac{1}{5}$; Pixel size: $1''.23 \text{ px}^{-1}$	ELGIN
Las Cumbres Observatory, McDonald Observatory, TX, USA (a) 2018 Jun 20	16 inches (40 cm) FOV: $29' \times 19'$; Pixel size: $0''.57 \text{ px}^{-1}$	LCOGT-MDO
Las Cumbres Observatory, Observatorio del Teide, Tenerife, Spain (a) 2018 Jun 25, (b) 2018 Aug 7, (c) 2018 Aug 30, (d) 2018 Sep 19	16 inches (40 cm) FOV: $29' \times 19'$; Pixel size: $0''.57 \text{ px}^{-1}$	LCOGT-OT

Note. Letters beneath each observatory indicate the dates of observation (see Figure 3). The field of view (FOV) in arcminute and pixel scale in arcsecond are also indicated.

least dispersed residuals. Using the RVs obtained from the G2 mask does not significantly change our results. Similarly, the measured CCF bisector spans quantify possible shape variations of the spectral lines. They show no correlations with the RVs, and no significant variations: their dispersion is two times smaller than the RV dispersion, whereas each bisector span is roughly one-half as precise as the corresponding RV measurement. This reinforces the conclusion that the RV variations are due to a planetary companion, and not caused by spectral-line profile changes attributable to blends or stellar activity.

4. Analysis

4.1. Spectral Analysis of the Host Star

We begin our analysis of the data with a study of the host star. Stellar atmospheric parameters (T_{eff} , $\log g$, and $[\text{Fe}/\text{H}]$) and respective uncertainties were derived using the methodology described in Sousa et al. (2008) and Santos et al. (2013). In brief, we make use of the equivalent widths of tens of iron lines and we assume ionization and excitation equilibrium. The process makes use of a grid of Kurucz model atmospheres (Kurucz 1993) and the radiative transfer code MOOG (Snedden 1973).

The equivalent widths were measured on a SOPHIE spectrum built from the addition of the spectra used for the RV measurements, but excluding the five SOPHIE spectra presenting moonlight contamination. We obtained $T_{\text{eff}} = 6220 \pm 70 \text{ K}$, $\log g = 4.2 \pm 0.1$ (cgs), and $[\text{Fe}/\text{H}] = +0.48 \pm 0.05$. Using the calibration of Torres et al. (2010) with a correction following Santos et al. (2013), we derive a mass and radius of $1.43 \pm 0.09 M_{\odot}$ and $1.47 \pm 0.20 R_{\odot}$, respectively. We also derived the projected rotational velocity $v \sin i = 6 \pm 1 \text{ km s}^{-1}$ from the parameters of the CCF using the calibration of Boisse et al. (2010).

4.2. Combined Fit

Proceeding to a comprehensive analysis of the system, we fit the photometric follow-up light curves and the radial velocities together using EXOFASTv2 (Eastman et al. 2019). In each light curve, we verified that the uncertainties of individual data points were of the same order as the standard deviation of the light curve (after subtracting the transit), to ensure that they

were not under- or overestimated. In some cases, we rescaled the uncertainties accordingly. We used MIST stellar isochrones (Choi et al. 2016; Dotter 2016; Paxton et al. 2011, 2013, 2015), a spectral energy distribution (SED) constructed from Tycho (Høg et al. 2000), 2MASS (Cutri et al. 2003; Skrutskie et al. 2006), and WISE (Cutri et al. 2014) catalog magnitudes, and the *Gaia* DR2 parallax (Gaia Collaboration et al. 2018) for BD +85 317 to constrain the host star’s parameters. We use a quadratic limb-darkening law:

$$\frac{I_{\mu}}{I_0} = 1 - u_1(1 - \mu) - u_2(1 - \mu)^2 \quad (1)$$

where I is the intensity and μ is the angle between a line normal to the stellar surface and the line of sight of the observer. The limb-darkening coefficients u_1 and u_2 are free parameters with theoretical values interpolated from updated Claret (2017) tables. In the fit, we set four priors: we used the SOPHIE spectral analysis to constrain the effective temperature and metallicity for the stellar isochrone fitting. We also set a prior on the *Gaia* parallax with an updated uncertainty (see Section 4.3). Finally, we used Schlafly & Finkbeiner (2011) measurements to place an upper limit on *V*-band extinction (see also Green et al. 2019). We set unconstrained starting values (e.g., transit depth and duration) based on the posteriors of a brief fitting run. In the full Markov Chain Monte Carlo (MCMC) analysis, we simultaneously fit a model to the transits and RVs, including a linear fit to the long-term trend from the latter data. The chains were well mixed (Gelman–Rubin statistic < 1.01) after $\sim 37,000$ steps.

The final parameter values and their uncertainties are computed as the medians and 1σ values of their respective posterior distribution functions. The limb-darkening coefficients are free and are treated in the same way as other parameters. We also ran a zero-eccentricity model to the data and find no significant changes in the final parameters.

The residual RVs are consistent with zero after subtracting the best-fit hot Jupiter signal and the long-term trend containing the systemic velocity. We found an RV jitter of $8.1 \pm 3.3 \text{ m s}^{-1}$ during the MCMC. We list the results from the fit in Tables 2–4.

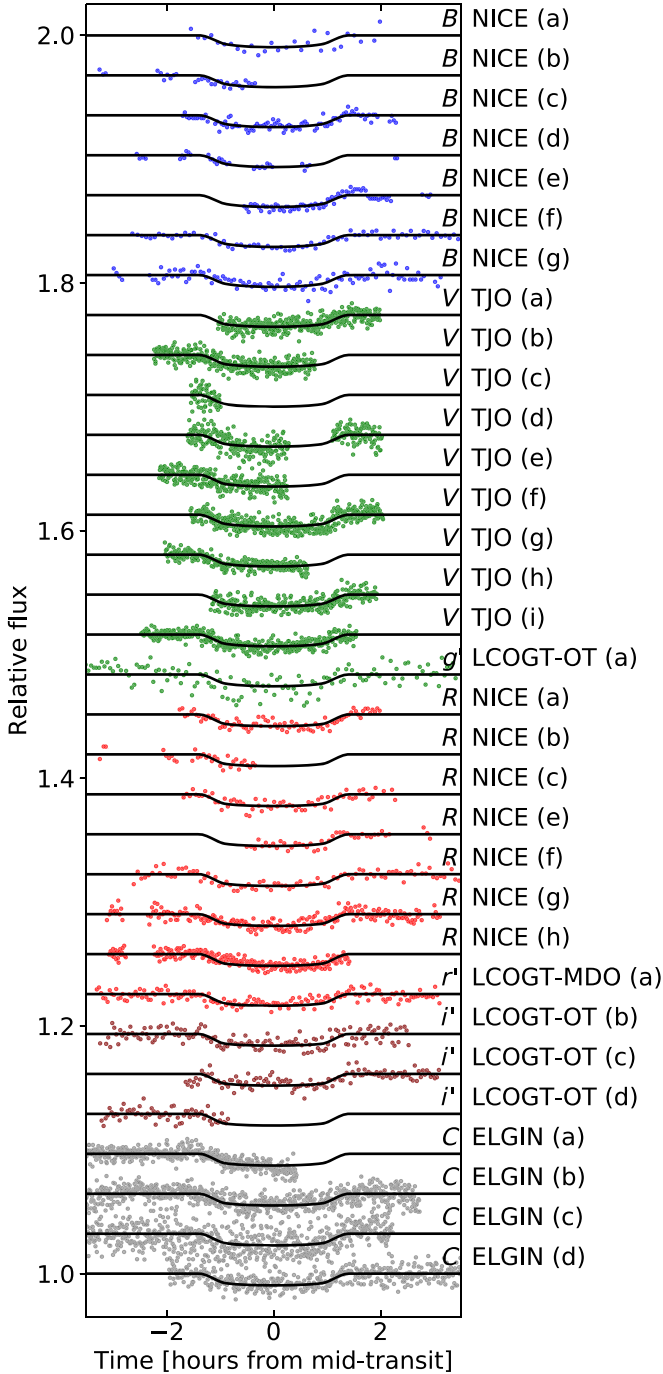


Figure 3. Photometric follow-up of XO-7 b. Individual transits are displayed. Bandpasses are noted B (blue), V and g' (green), R and r' (red), i' (dark red), and C (gray); observatories and observation dates are labeled as in Table 1. The best transit model calculated in each bandpass is overplotted as a black line. The light curves do not have the same time sampling; thus, the apparent point-to-point dispersion is not representative of their relative quality. Light curves are offset for clarity.

4.3. Analysis of Gaia DR2 Data

Gaia DR2 data can be used to constrain exoplanet system parameters. In our combined fit, we used the *Gaia* DR2 parallax as an input. As a case study, we discuss the validity of this measurement using *Gaia* quality indicators and other studies.

There are a number of indications that the *Gaia* DR2 astrometry for this star is reliable. Its proper motion and parallax

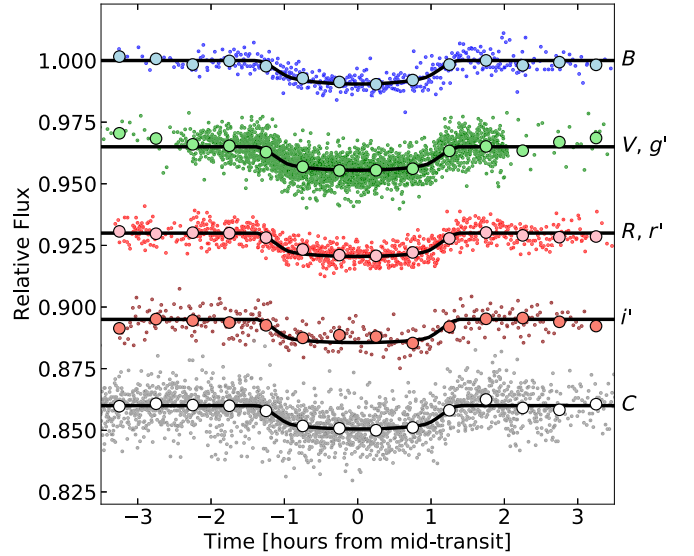


Figure 4. Photometric follow-up observations of XO-7 b gathered by bandpasses: B (blue), V and g' (green), R and r' (red), i' (dark red), and C (gray) from top to bottom. Data from different observations are blended in their respective filter bands. The best transit model in each bandpass is overplotted as a black line. We also plot the median flux values of bins spaced by 30 minutes for each lightcurve. Lightcurves are offset for clarity.

from *Gaia* DR2, *Gaia* DR1, and Tycho-2 are in full agreement. There is no nearby bright source: the nearest Tycho-2 star is more than $99''.9$ away ($\text{prox} = 999$). There is no indication from *Gaia* DR1 of a long-term curvature of the proper motion that could be caused by a companion ($\text{astrometric_delta_q} = 0.00$). The ecliptic latitude of the star ($\beta = 71^\circ 28'$) is in general good for astrometry, as confirmed by the *Gaia* DR2 statistics: 219 of the 227 observations (called “transits”) have been used in the astrometric solution, distributed over 18 visibility periods, far above the minimum number of five periods required. The mean parallax factor is normal ($\text{mean_varpi_factor_al} = 0.040$), indicating that the astrometric fit should be straightforward, and the astrometric excess noise is zero ($\text{astrometric_excess_noise} = 0.000$ mas), which confirms the high quality of the *Gaia* DR2 astrometry. One suspicious element is the duplicate source flag ($\text{duplicated_source} = 1$). However, the number of “transits” is similar to that of the nearby faint star (Section 3.1), which has a duplicate source flag of 0. This precludes that the second, duplicated, source identifier is hiding large amounts of data; thus the *Gaia* DR2 astrometry is based on most data. The astrometric goodness of fit is poor ($\text{astrometric_gof_al} = 9.9804$), but the Revised Unit Weight Error (which is a rescaled astrometric quality indicator) is 1.12, which is lower than the threshold of 1.4 that indicates suspicious astrometry. The duplicate source flag likely originates from the partial saturation of this object.

Lindgren et al. (2018a, 2018b) state that the DR2 error for *Gaia* parallaxes does not represent the total uncertainty. We increased the uncertainty of the XO-7 parallax using the calibration formula given in slide 17 of Lindgren et al. (2018b; see “Known issues with the *Gaia* DR2 data”²¹). We also considered a systematic offset in the *Gaia* DR2 parallax of XO-7. Hall et al. (2019) provide a compilation of literature values in addition to their own finding and report a systematic offset around $-50 \mu\text{as}$ (see their Figure 8, Tables 9 and 10). We ran our

²¹ <https://www.cosmos.esa.int/web/gaia/dr2-known-issues>

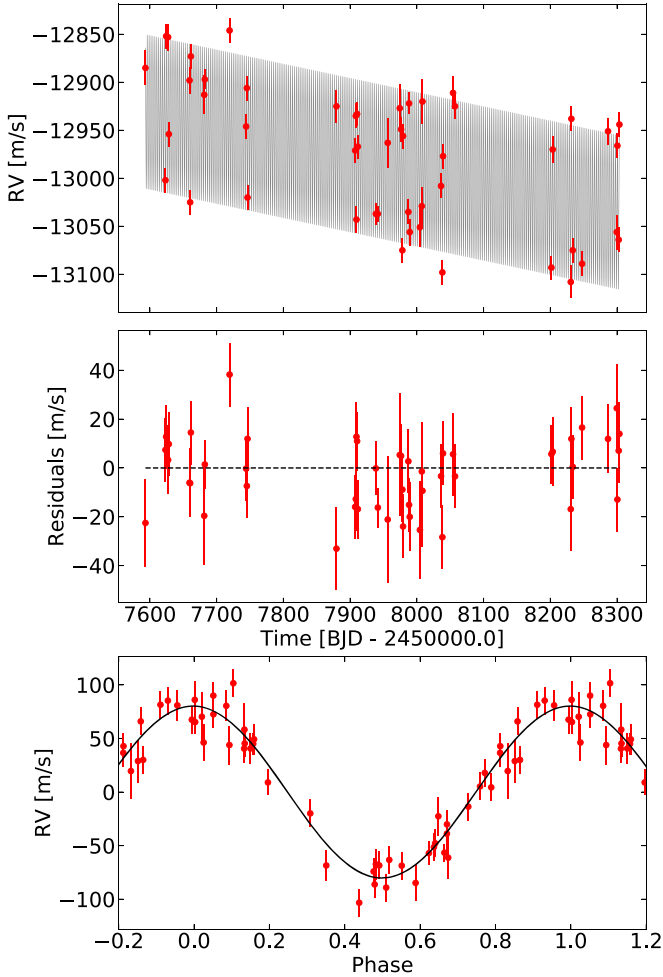


Figure 5. SOPHIE radial velocities of XO-7 with 1σ error bars (red). In the top panel, the gray area represents a circular Keplerian fit to the hot-Jupiter-induced motion combined with a linear trend for the unseen companion. The middle panel shows the residuals. In the bottom panel, we plot the RVs and model fit with the linear trend subtracted, phase-folded at the hot Jupiter’s orbital period.

analysis for two extreme cases: no offset and a $-82 \pm 33 \mu\text{s}$ offset as found by Stassun & Torres (2018), propagating the uncertainties accordingly. The largest discrepancy between best-fit parameters from the two analyses was a 1σ difference in the stellar radius. Because the posterior values do not significantly change after the systematic parallax correction, we used the original *Gaia* DR2 parallax value and the calibrated uncertainty in our final analysis.

The effective temperature given by *Gaia* DR2 ($T_{\text{eff}} = 5877 [5706, 6031] \text{ K}$) is lower than the one we measure from high-resolution spectroscopy (the values in brackets are the 16th and 84th percentiles of the probability density function). The radius from *Gaia* DR2 based on the *BP* and *RP* magnitudes ($R = 1.58 [1.51, 1.68] R_{\odot}$) is slightly larger than inferred from our fit. *Gaia* values are useful for ensemble analysis but are not necessarily accurate for single objects. The system RV from *Gaia* DR2 ($V_{\text{sys}} = -12.82 \pm 0.44 \text{ km s}^{-1}$) is in excellent agreement with our measurement.

4.4. Secondary Eclipse

We do not detect the secondary eclipse in the XO light curve. We set an upper limit on its depth δ_e in the XO bandpass by calculating the noise in the folded light curve. We eliminate

Table 2
Parameters of the Planet Host Star

Quantity	Unit	Value	Notes
Name		BD+85 317	1
R.A.	J2000	18:29:54.929	2
decl.	J2000	+85:13:59.58	2
p	mas	4.2419 ± 0.0215	2
d	pc	234.1 ± 1.2	3
μ_{α}	mas yr^{-1}	-15.354 ± 0.038	2
μ_{δ}	mas yr^{-1}	24.461 ± 0.054	2
γ	km s^{-1}	-12.983 ± 0.015	7
B	mag	11.23 ± 0.06	4
V	mag	10.52 ± 0.04	4
G	mag	10.4575 ± 0.0004	2
J	mag	9.557 ± 0.024	5
H	mag	9.308 ± 0.030	5
K	mag	9.241 ± 0.024	5
BP	mag	10.7795 ± 0.0008	2
RP	mag	10.0087 ± 0.0010	2
$BP - RP$	mag	0.7707	2
AG	mag	$0.6980 [0.5709 \ 0.8174]$	2, 8
$E(BP - RP)$	mag	$0.3450 [0.2543 \ 0.4170]$	2, 8
Sp Type		G0V	6
T_{eff}	K	6250 ± 100	7
[Fe/H]	dex	0.432 ± 0.057	7
$\log g$	cgs	4.246 ± 0.023	7
$v \sin i$	km s^{-1}	6 ± 1	7
M	M_{\odot}	1.405 ± 0.059	7
R	R_{\odot}	1.480 ± 0.022	7
Age	Gyr	$1.18^{+0.98}_{-0.71}$	7
RV slope	$\text{m s}^{-1} \text{ day}^{-1}$	-0.148 ± 0.011	7

Note. (1): Argelander (1903), (2): Gaia Collaboration et al. (2018), (3): Bailer-Jones et al. (2018), (4): Høg et al. (2000), (5): Cutri et al. (2003), (6): Pickles & Depagne (2010), (7): This work, (8): The values in brackets are the 16th and 84th percentiles of the probability density function.

the in-transit points, fold the light curve at 10^5 different periods ranging from 2 to 3.7 days, split each light curve into segments equal to the eclipse duration (assumed to be equal to the transit duration), and calculate the mean flux in each segment. This yields the distribution of flux variations over the timescale of the eclipse. We take the 3σ values of this distribution as the 3σ upper limit on δ_e . We find $\delta_e < 0.00142$ at 3σ in the *R* band. This limit is too high to constrain the brightness temperature and albedo of the planet’s day side.

4.5. Transit Timing Variations

We measure the central times t_c of individual transits that were observed during the follow-up campaign. We do not find any correlation pattern between the t_c and the period index of the transits, calculated as the number of orbital periods after the first transit. We put an upper limit on the presence of transit timing variations (TTVs) by measuring the standard deviation of the distribution of t_c : TTVs of XO-7b should be lower than 5 minutes at 1σ (15 minutes at 3σ) over the two years of observations. This is consistent with the fact that our RV measurements rule out the presence of companions massive and close enough to induce significant TTVs on shorter timescales. We note that measuring TTVs from ground-based observations that are affected by correlated noise is challenging, as studied by Carter & Winn (2009).

5. System Parameters

In this section, we list the parameters of the host star and hot Jupiter as determined by the preceding analysis. We also report the presence of a wide-orbit companion implied by a slope in the RV measurements.

5.1. Stellar Parameters

The host star is BD+85 317 and is classified as G0V (Pickles & Depagne 2010), sometimes G2 (Wright et al. 2003). Its parameters are reported in Table 2. It is bright and circumpolar (within 5° of the celestial north pole), which could facilitate follow-up observations from the northern hemisphere. It has a high metallicity that is among the highest for stars harboring a hot Jupiter. Its age estimated from the best-fit MIST isochrone in the $T_{\text{eff}} - \log g$ space indicates that it is relatively young. However, several isochrones of disparate ages are in close proximity and provide a good fit as reflected by the large uncertainty (nearly 100%). Thus, the age should be taken with caution and further study such as activity indicator analysis would be necessary for a better estimate. If indeed the star is young, XO-7 b would be one of the very few hot Jupiters known around young stars.

5.2. Hot Jupiter Parameters

The hot Jupiter has an orbital period of 2.864 days, a mass of $0.709 \pm 0.034 M_J$, and a radius of $1.373 \pm 0.026 R_J$, yielding a density of $0.340 \pm 0.027 \text{ g cm}^{-3}$. At a distance of $0.04421 \pm 0.00062 \text{ au}$ from its star, the planet has an equilibrium temperature of $1743 \pm 23 \text{ K}$ assuming a zero albedo. The orbit is consistent with being circular. The parameters of the hot Jupiter are reported in Table 3 and the best-fit limb-darkening coefficients for each band are reported in Table 4.

5.3. Wide-Orbit Companion

The RV measurements show a linear trend in addition to the radial velocities induced by the hot Jupiter, indicating the presence of a wide-orbit companion. The secular change is 100 m s^{-1} over two years and no curvature is apparent in the data. Thus, the minimum orbital period is four years in the case of a circular orbit and two years for a very eccentric orbit. Assuming a circular orbit, we derive a minimum mass of $4 M_J$ for the companion, which could be a planet, a brown dwarf, or a star. This system is still under monitoring to characterize the long-period companion.

6. Discussion

6.1. Prospects for Atmospheric Characterization

XO-7 b is an inflated hot Jupiter and is moderately hot. Its large atmospheric scale height ($H = 671 \text{ km}$), combined with the brightness of the host star, makes it well suited to atmospheric characterization. It is among the 25 known transiting hot Jupiters with an atmospheric scale height larger than 500 km and a host star brighter than magnitude 11 in the V band. Assuming an absorption spanning two scale heights and estimating the amplitude of the transmission signal by $2H \times 2R_p/R_\star^2$, we expect a signal of 250 ppm, which could be detected with *Hubble Space Telescope* (HST; Figure 6). Thus, XO-7 b is a valuable target to investigate the atmospheric properties of moderately irradiated close-in gas giant planets.

Table 3
Median Values and 68% Confidence Intervals for XO-7 b

Quantity	Unit	Value
P	Period (day)	2.8641424 ± 0.0000043
R_p	Radius (R_J)	1.373 ± 0.026
T_C	Time of conjunction (BJD _{TDB})	$2457917.47503 \pm 0.00045$
a	Semimajor axis (au)	0.04421 ± 0.00062
i	Inclination (degrees)	83.45 ± 0.29
e	Eccentricity	0.038 ± 0.033
T_{eq}	Equilibrium temperature (K)	1743 ± 23
M_p	Mass (M_J)	0.709 ± 0.034
K	RV semi-amplitude (m s^{-1})	80.5 ± 3.2
R_p/R_\star	Radius of planet in stellar radii	0.09532 ± 0.00093
a/R_\star	Semimajor axis in stellar radii	6.43 ± 0.14
δ	Transit depth (fraction)	0.00909 ± 0.00018
τ	Ingress/egress transit duration (day)	0.0190 ± 0.0015
T_{14}	Total transit duration (day)	0.1155 ± 0.0014
T_{FWHM}	FWHM transit duration (day)	0.09655 ± 0.00074
b	Transit impact parameter	0.709 ± 0.023
$\delta_{S,3.6}$	Blackbody eclipse depth at $3.6 \mu\text{m}$ (ppm)	898 ± 29
$\delta_{S,4.5}$	Blackbody eclipse depth at $4.5 \mu\text{m}$ (ppm)	1150 ± 34
ρ_p	Density (cgs)	0.340 ± 0.027
$\log g_p$	Surface gravity	2.970 ± 0.028
Θ	Safronov Number	0.0325 ± 0.0014
$\langle F \rangle$	Incident Flux ($10^9 \text{ erg s}^{-1} \text{ cm}^{-2}$)	2.09 ± 0.11
T_S	Time of eclipse (BJD _{TDB})	2457918.900 ± 0.029
M_p/M_\star	Mass ratio	0.000482 ± 0.000021
P_T	A priori non-grazing transit prob	0.1457 ± 0.0073
$P_{T,G}$	A priori transit prob	0.1764 ± 0.0087

Table 4
Best-fit Limb-darkening Coefficients using a Quadratic Law

Band	u_1	u_2
B	0.586 ± 0.031	0.213 ± 0.026
V	0.404 ± 0.024	0.296 ± 0.019
g'	0.504 ± 0.054	0.250 ± 0.052
R	0.317 ± 0.024	0.321 ± 0.020
r'	0.340 ± 0.052	0.313 ± 0.050
i'	0.252 ± 0.032	0.312 ± 0.029
C	0.352 ± 0.029	0.311 ± 0.026

Among known transiting hot Jupiters with a mass, radius, and equilibrium temperature within 20% of those of XO-7 b, two have been observed in spectroscopy with *HST* STIS and/or WFC3: HD 209458 b and HAT-P-13 b. Atomic and molecular species have been detected in the atmosphere of HD 209458 b, including water vapor signatures around $1.4 \mu\text{m}$ with an amplitude of 200 ppm, which is about twice smaller than expected for a clear, solar-composition atmosphere, and indicates extra absorption by haze and/or dust (Deming et al. 2013; Sing et al. 2016). This low amplitude might also be due to a depletion in oxygen compared to solar abundance (Madhusudhan et al. 2014), although this explanation is not favored at the moment. The HAT-P-13 b WFC3 observations have not been published but are available on the MAST archive. Observing XO-7 b in transit spectroscopy would test if the atmospheric properties measured for HD 209458 b are also valid for a planet with similar characteristics and would help constrain hot Jupiter atmosphere models.

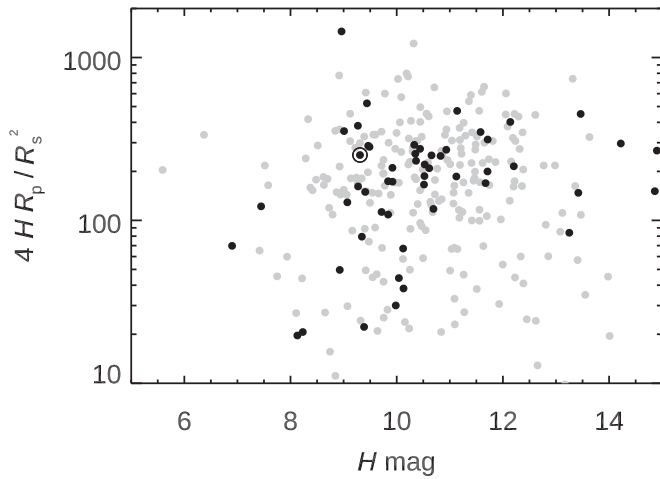


Figure 6. Estimated planetary atmospheric transmission signal as a function of host star H magnitude for known transiting hot Jupiters (defined as $0.3 M_J < M_p < 13 M_J$ and $P < 20$ days). Host stars visible by *JWST* more than 200 days per year are shown in black. XO-7 is highlighted by a black open circle. Data are from exoplanet.eu, simbad.u-strasbg.fr, and the *JWST* General Target Visibility Tool.

The host star has a high ecliptic latitude ($\beta = 71^\circ 28'$) and will be visible during a continuous period of 212 days with *JWST*. In addition, it is bright but will not saturate the *JWST* detectors in time-series spectroscopic observation modes (except in the NIRSpec PRISM/CLEAR configuration) and there is no surrounding star that could contaminate the spectrum (the faint nearby star is far enough away). Thus, it is an excellent target for *JWST*. It will also be a good target for ARIEL for similar reasons: it will be visible continuously, it is bright, and the presence of the companion makes it valuable as part of a larger sample to investigate connections between formation and migration mechanisms and atmospheric compositions. Thus, it would be a good addition to the ARIEL target list.

6.2. Prospects from TESS Follow-up

The transiting extrasolar planet XO-7 b reported here is probably the last of the series discovered by the XO project (McCullough et al. 2005). This section addresses some of the ways in which data from a ground-based survey such as XO differ from data from the *TESS* mission.²² Comparison of XO data for XO-7 b and *TESS* data for a similar planet (WASP-126b) demonstrates that, for discovering transiting planets, *TESS* data will be far superior. *TESS* is observing XO-7 as TIC 268403451 in camera 3 during its Sectors 18–20, between 2019 November and 2020 January. The *TESS* light curve will consist of nearly continuous monitoring of XO-7 for three months at 2 minutes cadence. For comparison, we selected an exoplanet candidate (TIC 25155310; TOI-114.01) with similar properties to XO-7/XO-7 b from the many candidates already reported by *TESS*. Like XO-7 b, the example that we selected happens to be a rediscovery by *TESS* of a planet, WASP-126b, discovered by a ground-based survey. Whereas XO-7 b transits a $V = 10.5$ mag G0 V star every 2.9 days, WASP-126b transits a $V = 10.8$ mag G2 V star every 3.3 days (Maxted et al. 2016). We

obtained a *TESS* data validation report for WASP-126b from MAST²³ that includes 21 transits observed during *TESS* sectors 1–3. WASP-126b’s transit depth is reported as 7182 ± 39 ppm.

Detection of the secondary eclipse of XO-7 b would permit a measure of the superposition of reflected starlight and emission from the planet’s illuminated side. It would also confirm whether the orbital eccentricity is indeed close to zero. Unfortunately, the prospects are very poor for detecting the secondary eclipse of XO-7 b with *TESS* data. Based on the reported uncertainty of the depth of WASP-126b’s transit, a secondary eclipse of similar duration would have been marginally detected by *TESS* at 3σ if its depth were 117 ppm. However, if the geometric albedo of XO-7 b is typical of hot Jupiters, e.g., 0.1, then its secondary eclipse depth due solely to reflected light is expected to be 21 ppm (Sheets & Deming 2017, Equation (4)). While thermal emission from a hot Jupiter can contribute to the depth of its secondary eclipse, even within the 600–1000 nm bandpasses of *TESS* or *Kepler*, Sheets & Deming (2017, Table 4) report a median of 35 ppm and a maximum of 91 ppm for the depths of secondary eclipses of 14 hot Jupiters. Because those two estimates of secondary eclipse depths (21 ppm and 35 ppm) are much smaller than the 117 ppm estimate of a marginal (3σ) detection of such an eclipse with *TESS* data similar to that expected for XO-7, we expect that *TESS* will not detect XO-7 b’s secondary eclipse.

Similarly, a search of *TESS* data of XO-7 could turn up transits of a planet smaller in radius than XO-7 b. However, such a search is likely to be fruitless because such companions to hot Jupiters are rare (Steffen et al. 2012). Likewise, measuring XO-7’s mean density or age from asteroseismology will not be possible with *TESS* data: XO-7 is a few magnitudes too faint (see Campante et al. 2016, Figure 12(a)). *TESS* photometry may enable measuring the rotation period of the star XO-7 and comparing XO-7’s rotation period and its radius with its spectroscopically determined $v \sin(i)$ may yield the star’s spin-axis inclination (i) for comparison with the projected angle of orbital obliquity of XO-7 b inferred from the Rossiter–McLaughlin effect (Holt 1893; McLaughlin 1924; Rossiter 1924). For stars hotter than approximately 6250 K, the pole of the planet’s orbit could be preferentially misaligned with respect to the stellar spin axis (Winn et al. 2010a); XO-7’s effective temperature (6250 ± 100 K; Table 2) places it at the threshold.

6.3. Follow-up of the Wide-orbit Companion

The secular trend in XO-7’s radial velocities indicates an unseen companion, either a planet, brown dwarf, or star. Ngo et al. (2016) estimate that the hosts of hot Jupiters have stellar companions with separations less than 50 au in $3.9^{+4.6}_{-2.0}\%$ of their sample. Knutson et al. (2014) estimate that $27\% \pm 6\%$ of hot Jupiters have a planetary companion in the range of mass 1–13 M_J and semimajor axis 1–10 au. In absolute value, the slope of XO-7’s radial velocities, $-0.148 \pm 0.001 \text{ m s}^{-1} \text{ day}^{-1}$, is 1.5 times larger than the maximum slope ($-0.097 \pm 0.023 \text{ m s}^{-1} \text{ day}^{-1}$) exhibited in a sample of 51 hot Jupiters observed by Knutson et al. (2014), typically for at least five years each.²⁴ The slope of XO-7’s radial velocities implies the following relationship

²² In this section, we assume that *TESS* will complete its two-year survey nominally (with shifted sectors 14, 15, and 16 in Cycle 2) and, except where noted, extensions of the *TESS* primary mission will not be required to obtain the results discussed.

²³ <https://archive.stsci.edu/prepds/teess-data-alerts/#dataaccess>

²⁴ This statement ignores the three systems for which inflexions enabled a two-planet solution: HAT-P-17, WASP-8, WASP-34.

between the unseen companion’s mass (M_c , in solar units) and its angular separation from XO-7 (θ , in arc seconds; Knutson et al. 2014, Equation (1)):

$$M_c = 40 \theta^2, \quad (2)$$

which implies that the companion must be hidden within a nominal ground-based seeing disk ($2''$ FWHM), otherwise it would be much more massive than XO-7 and would dominate the light. If it is a low-mass star ($0.1\text{--}0.4 M_\odot$), then its separation is $0''.05\text{--}0''.1$, or $12\text{--}24$ au, and could be revealed, with adaptive optics as a main-sequence M star, respectively $7\text{--}4$ mag fainter than XO-7 in K band (Delfosse et al. 2000, Figure 1).

Regardless of whether it is a planet, brown dwarf, or a star, if its orbit is not very elliptical, then its orbital period must be measured in years, otherwise the trend of radial velocities would show some degree of curvature. For example, a $M \sin(i) = 5 M_J$ companion in a five-year circular orbit is consistent with the radial velocities measured to date. In that case, *Gaia* astrometry would be able to detect at $\sim 5\sigma/\sin(i)$ the $\sim 50/\sin(i)$ micro-arcsecond astrometric wobble of XO-7 induced by such a companion (Perryman et al. 2014). Astrometric orbits from *Gaia* will be available in DR4. Combining the astrometric orbit of XO-7 with our RV measurements will allow us to reconstruct the orbits in three dimensions and measure the mass of the wide-orbit companion. If it is stellar, the companion may also be detected in photometry by *Gaia* (de Bruijne et al. 2015). Companions at such small separations are very incomplete in *Gaia* DR2 and need special ground processing (Arenou et al. 2018); they will be available in *Gaia* DR4.

6.4. Migration and Orbit of the Hot Jupiter

Hot Jupiters are thought to form beyond the water ice line and migrate inward to reach close-in orbits. Two mechanisms have been proposed: disk or high-eccentricity migration. Disk migration should yield orbits that are circular and contained in the plane perpendicular to the star rotation axis, and can go on until the planet reaches the Roche limit a_{Roche} . In contrast, high-eccentricity migration should yield a wide range of obliquities and the planet is expected to reach a circular orbit at a distance almost exactly $2 a_{\text{Roche}}$ (Faber et al. 2005). The orbit may also retain some eccentricity depending on the circularization timescale. In this process, the initial eccentricity can originate from scattering interactions with another massive companion. Although no correlations have been found between hot Jupiter orbital parameters and the presence of distant companions (Knutson et al. 2014), we place XO-7 in the context of these mechanisms. XO-7 has an outer companion of at least $4 M_J$ and the hot Jupiter appears to have a nearly circular orbit. We calculate the Roche limit of the star–hot Jupiter system as $a_{\text{Roche}} = 2.7 R_p (M_*/M_p)^{1/3}$ and find $a_{\text{Roche}} = 0.023$ au. Interestingly, the semimajor axis is almost twice the Roche limit ($a/a_{\text{Roche}} = 1.95$). This is consistent with expectations for high-eccentricity migration (although disk migration is not ruled out). As illustrated in Figure 8 of Sarkis et al. (2018), almost all transiting hot Jupiters with a massive outer companion have $a/a_{\text{Roche}} > 2$. One exception has a/a_{Roche} just below 2, as for XO-7 b. Overall, this supports high-eccentricity migration for hot Jupiters in these systems.

If the planet–planet scattering mechanism played a role in the formation of this system, then we can expect a non-zero obliquity for the hot Jupiter. The wide-orbit companion may

also affect the hot Jupiter’s orbit via the Lidov–Kozai mechanism (Kozai 1962; Lidov 1962), which has been proposed to explain the observed sky-projected obliquities of hot Jupiters (Schlaufman 2010; Winn et al. 2010a; Albrecht et al. 2012; Dawson & Chiang 2014; Winn & Fabrycky 2015). Our attempts to observe the Rossiter–McLaughlin effect during a transit of XO-7 b to measure its obliquity have been unsuccessful so far, but we plan to make this observation in the near future. This will bring another clue to understand the formation, migration, and architecture of the XO-7 system.

6.5. Similarities between XO-7 and HAT-P-13

The XO-7 system has striking similarities with HAT-P-13 (Bakos et al. 2009; Winn et al. 2010b). The two hot Jupiters XO-7 b and HAT-P-13 b have, respectively, similar periods (2.86 and 2.92 days), masses (0.71 and $0.85 M_J$), radii (1.37 and $1.27 R_J$), semimajor axes (0.044 and 0.043 au), and equilibrium temperatures (1747 and 1653 K); the host stars XO-7 and HAT-P-13 are metal-rich G dwarfs with similar metallicities (0.43 and 0.41 dex), and both have a second companion on a wide orbit. HAT-P-13 c is well characterized ($P = 446.27 \pm 0.22$ days, $M \sin i = 14.28 \pm 0.28 M_J$, $e = 0.6616 \pm 0.0054$) whereas XO-7 is still under monitoring to characterize that companion. HAT-P-13 has a third outer companion revealed by a linear trend in radial velocities (Winn et al. 2010b; Knutson et al. 2014). XO-7 b and HAT-P-13 b have radius ratios a/a_{Roche} of 1.96 and 2.27 and both have a nearly zero eccentricity (0.036 ± 0.032 and 0.0133 ± 0.0041). These systems have different ages ($1.12^{+0.94}_{-0.66}$ and $5.0^{+2.5}_{-0.7}$ Gyr). It would be interesting to investigate if they could have formed in the same way. Also, comparing the XUV emission of the stars, for example, with the He I $1.08 \mu\text{m}$ absorption feature of the hot Jupiter’s atmospheres with high-resolution spectroscopy could provide clues on evaporation scenarios of these atmospheres (e.g., Allart et al. 2018; Nortmann et al. 2018). Finally, both stars are metal-rich and host at least two massive companions, and it is known that giant planet formation is correlated with stellar metallicity (Fischer & Valenti 2005). On the other hand, no statistically significant correlation between the frequency of long-period companions and stellar metallicity has been found in hot Jupiter systems (Knutson et al. 2014). Thus, how to interpret these high metallicities in the context of the formation of these systems remains an open question.

7. Conclusion

We report the discovery of the transiting hot Jupiter XO-7 b orbiting a main-sequence G0 star. Its bright host star and large atmospheric scale height make it well suited to atmospheric characterization. Its physical properties are close to those of HD 209458 b, which has been extensively characterized, and even closer to HAT-P-13 b. Inferring whether their atmospheres also have similar properties would help constrain hot Jupiter atmosphere models. The object is circumpolar, which could facilitate follow-up observations from the ground. We detect the presence of a more massive, wide-orbit companion with a period of at least a few years. RV monitoring is underway to determine whether this companion is a planet, a brown dwarf, or a low-mass star. In addition, the astrometric motion of the host star caused by that companion should be detectable by *Gaia* and available in DR4. Combining these measurements will yield the orbits in three dimensions. If it is a

low-mass star, that companion may also be seen in adaptive optics imaging. *TESS* photometry of XO-7 will yield improved parameters of the hot Jupiter and host star and may provide the star's rotation period, from which we could determine its spin-axis inclination. Measuring the Rossiter–McLaughlin effect in radial velocities will yield the hot Jupiter's obliquity and a potential link with the wide-orbit companion may be investigated. Finally, the hot Jupiter orbital parameters and the presence of a wide-orbit companion are consistent with expectations for a high-eccentricity migration mechanism. Thus, this discovery is valuable to investigate the formation and evolution of hot Jupiter systems.

We thank the anonymous referee for helpful thoughts and critique that strengthened our paper. We also thank the editor for overseeing our submission. The XO project is supported by NASA grant NNX10AG30G. I.R., F.V., and E.H. acknowledge support by the Spanish Ministry for Science, Innovation and Universities (MCIU) and the Fondo Europeo de Desarrollo Regional (FEDER) through grant ESP2016-80435-C2-1-R, as well as the support of the Generalitat de Catalunya/CERCA programme. The Joan Oró Telescope (TJO) of the Montsec Astronomical Observatory (OAdM) is owned by the Generalitat de Catalunya and operated by the Institute for Space Studies of Catalonia (IEEC). N.C.S. was supported by FCT-Fundação para a Ciência e a Tecnologia through national funds and by FEDER-Fundo Europeu de Desenvolvimento Regional through COMPETE2020-Programa Operacional Competitividade e Internacionalização by these grants: UID/FIS/04434/2019; PTDC/FIS-AST/28953/2017 & POCI-01-0145-FEDER-028953 and PTDC/FIS-AST/32113/2017 & POCI-01-0145-FEDER-032113. H.P.O. acknowledges support from Centre National d'Etudes Spatiales (CNES) grant 131425-PLATO. This research made use of Photutils, an Astropy package for detection and photometry of astronomical sources (Bradley et al. 2019). This research has made use of the Exoplanet Orbit Database and the Exoplanet Data Explorer at exoplanets.org, the Extrasolar Planets Encyclopaedia at exoplanet.eu, and the SIMBAD and VizieR databases at simbad.u-strasbg.fr/simbad/ and <http://vizier.u-strasbg.fr/viz-bin/VizieR>.

Facilities: OHP (SOPHIE), LCOGT:0.4 m, Montsec Astronomical Observatory:Joan Oró Telescope, Nice Observatory: Schaumasse.

Software: astrometry.net (Lang et al. 2010), Stellar Photometry Software (Janes & Heasley 1993), IRIS (Buil 2005), ICAT (Colome & Ribas 2006), AstroImageJ (Collins et al. 2017), Photutils (Bradley et al. 2019), JKTLTD (Southworth 2015), EXOFASTv2 (Eastman et al. 2019).

Appendix SOPHIE Radial Velocities

Table 5 provides the RV measurements of the host star XO-7 obtained with the SOPHIE spectrograph at the Observatoire de Haute-Provence, France, between 2016 July 23 and 2018 July 4.

Table 5

RV Measurements of the Host Star XO-7 Obtained with the SOPHIE Spectrograph



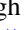

Reduced BJD	Orbital Phase	RV (km s ⁻¹)	σ (km s ⁻¹)
57593.3798	0.84405	-12.885	0.018
57623.3312	0.30141	-13.002	0.013
57624.3611	0.66100	-12.852	0.013

Table 5
(Continued)

Reduced BJD	Orbital Phase	RV (km s ⁻¹)	σ (km s ⁻¹)
57627.3535	0.70577	-12.853	0.014
57628.3640	0.05859	-12.954	0.013
57659.4151	0.89990	-12.898	0.014
57660.3593	0.22957	-13.025	0.013
57661.4453	0.60874	-12.873	0.013
57681.4732	0.60136	-12.913	0.020
57682.3493	0.90725	-12.897	0.010
57719.4319	0.85443	-12.846	0.013
57744.2203	0.50916	-12.946	0.013
57745.2956	0.88460	-12.906	0.013
57746.3182	0.24163	-13.020	0.013
57879.5980	0.77553	-12.925	0.017
57907.5616	0.53886	-12.971	0.013
57908.5474	0.88305	-12.935	0.013
57909.5485	0.23258	-13.043	0.014
57910.4944	0.56283	-12.933	0.012
57911.5923	0.94616	-12.967	0.012
57938.5932	0.37337	-13.037	0.011
57941.5753	0.41456	-13.037	0.008
57956.3772	0.58256	-12.963	0.026
57974.4250	0.88384	-12.927	0.025
57976.3684	0.56237	-12.949	0.013
57978.3666	0.26003	-13.075	0.013
57979.3836	0.61511	-12.956	0.013
57987.3315	0.39008	-13.035	0.013
57988.3711	0.75305	-12.922	0.011
57989.3676	0.10097	-13.056	0.014
58004.6152	0.42458	-13.051	0.020
58007.4696	0.42118	-13.029	0.020
58008.4712	0.77088	-12.920	0.023
58036.2733	0.47783	-13.008	0.013
58038.3084	0.18838	-13.098	0.013
58039.2630	0.52167	-12.977	0.013
58054.2434	0.75199	-12.911	0.017
58057.2494	0.80152	-12.925	0.013
58201.6742	0.22663	-13.093	0.012
58203.6295	0.90931	-12.970	0.014
58230.6347	0.33803	-13.108	0.017
58231.6159	0.68061	-12.938	0.013
58233.6379	0.38658	-13.075	0.013
58247.6194	0.26814	-13.089	0.013
58286.4787	0.83565	-12.951	0.014
58299.5470	0.39837	-13.056	0.018
58300.5370	0.74402	-12.966	0.013
58302.4766	0.42122	-13.064	0.013
58303.5649	0.80120	-12.944	0.013

Note. The orbital phase is 0 at mid-transit.

ORCID iDs

Nicolas Crouzet  <https://orcid.org/0000-0001-7866-8738>
 Brian F. Healy  <https://orcid.org/0000-0002-7718-7884>
 P. R. McCullough  <https://orcid.org/0000-0001-9165-9799>
 Ignasi Ribas  <https://orcid.org/0000-0002-6689-0312>

References

- Albrecht, S., Winn, J. N., Johnson, J. A., et al. 2012, *ApJ*, **757**, 18
 Allart, R., Bourrier, V., Lovis, C., et al. 2018, *Sci*, **362**, 1384
 Alsubai, K. A., Parley, N. R., Bramich, D. M., et al. 2013, *AcA*, **63**, 465
 Arenou, F., Luri, X., Babusiaux, C., et al. 2018, *A&A*, **616**, A17
 Argelander, F. W. A. 1903, *yCat*, **1122**, 0

- Baglin, A., Auvergne, M., Barge, P., et al. 2009, in IAU Symp. 253, *Transiting Planets*, ed. F. Pont, D. Sasselov, & M. J. Holman (Cambridge: Cambridge Univ. Press), 71
- Bailer-Jones, C. A. L., Rybizki, J., Fousneau, M., Mantelet, G., & Andrae, R. 2018, *AJ*, 156, 58
- Bakos, G., Noyes, R. W., Kovács, G., et al. 2004, *PASP*, 116, 266
- Bakos, G. Á., Csabry, Z., Penev, K., et al. 2013, *PASP*, 125, 154
- Bakos, G. Á., Howard, A. W., Noyes, R. W., et al. 2009, *ApJ*, 707, 446
- Baranne, A., Queloz, D., Mayor, M., et al. 1996, *A&AS*, 119, 373
- Berry, R., & Burnell, J. 2005, *The Handbook of Astronomical Image Processing*, Vol. 2 (Richmond, VA: Willmann-Bell)
- Boisse, I., Eggenberger, A., Santos, N. C., et al. 2010, *A&A*, 523, A88
- Bonomo, A. S., Santerne, A., Alonso, R., et al. 2010, *A&A*, 520, A65
- Borucki, W. J., Koch, D., Basri, G., et al. 2010, *Sci*, 327, 977
- Bouchy, F., Díaz, R. F., Hébrard, G., et al. 2013, *A&A*, 549, A49
- Bouchy, F., Hébrard, G., Udry, S., et al. 2009, *A&A*, 505, 853
- Bradley, L., Sipőcz, B., Robitaille, T., et al. 2019, *astropy/photutils*: v0.6, Zenodo, doi:10.5281/zenodo.2533376
- Buil, C. 2005, in *Digital Astrophotography: The State of the Art*, ed. D. Ratledge (Springer: London), 79
- Burke, C. J., McCullough, P. R., Valenti, J. A., et al. 2007, *ApJ*, 671, 2115
- Burke, C. J., McCullough, P. R., Valenti, J. A., et al. 2008, *ApJ*, 686, 1331
- Campante, T. L., Schofield, M., Kuzlewicz, J. S., et al. 2016, *ApJ*, 830, 138
- Carter, J. A., & Winn, J. N. 2009, *ApJ*, 704, 51
- Choi, J., Dotter, A., Conroy, C., et al. 2016, *ApJ*, 823, 102
- Claret, A. 2017, *A&A*, 600, A30
- Collier Cameron, A., Bouchy, F., Hébrard, G., et al. 2007, *MNRAS*, 375, 951
- Collins, K. A., Kielkopf, J. F., Stassun, K. G., & Hessman, F. V. 2017, *AJ*, 153, 77
- Colome, J., & Ribas, I. 2006, *IAUS*, 6, 11
- Crouzet, N. 2018, in *Handbook of Exoplanets*, ed. H. Deeg & J. Belmonte (Cham: Springer), 129
- Crouzet, N., McCullough, P. R., Long, D., et al. 2017, *AJ*, 153, 94
- Cutri, R. M., Skrutskie, M. F., van Dyk, S., et al. 2003, *yCat*, 2246, 0
- Cutri, R. M., Wright, E. L., Conrow, T., et al. 2014, *yCat*, 2328, 0
- Dawson, R. I., & Chiang, E. 2014, *Sci*, 346, 212
- de Bruijne, J. H. J., Allen, M., Azas, S., et al. 2015, *A&A*, 576, A74
- Delfosse, X., Forveille, T., Ségransan, D., et al. 2000, *A&A*, 364, 217
- Deming, D., Wilkins, A., McCullough, P., et al. 2013, *ApJ*, 774, 95
- Dotter, A. 2016, *ApJS*, 222, 8
- Eastman, J. D., Rodriguez, J. E., Agol, E., et al. 2019, arXiv:1907.09480
- Faber, J. A., Rasio, F. A., & Willems, B. 2005, *Icar*, 175, 248
- Fischer, D. A., & Valenti, J. 2005, *ApJ*, 622, 1102
- Gaia Collaboration, Brown, A. G. A., Vallenari, A., et al. 2018, *A&A*, 616, A1
- Green, G. M., Schlafly, E. F., Zucker, C., Speagle, J. S., & Finkbeiner, D. P. 2019, *ApJ*, 887, 93
- Hall, O. J., Davies, G. R., Elsworth, Y. P., et al. 2019, *MNRAS*, 486, 3569
- Hébrard, G., Bouchy, F., Pont, F., et al. 2008, *A&A*, 488, 763
- Høg, E., Fabricius, C., Makarov, V. V., et al. 2000, *A&A*, 355, L27
- Holt, J. R. 1893, *AstAp*, 12, 646
- Janes, K. A., & Heasley, J. N. 1993, *PASP*, 105, 527
- Johns-Krull, C. M., McCullough, P. R., Burke, C. J., et al. 2008, *ApJ*, 677, 657
- Knutson, H. A., Fulton, B. J., Montet, B. T., et al. 2014, *ApJ*, 785, 126
- Kovács, G., Zucker, S., & Mazeh, T. 2002, *A&A*, 391, 369
- Kozai, Y. 1962, *AJ*, 67, 579
- Kurucz, R. 1993, *ATLAS9 Stellar Atmosphere Programs and 2km⁻¹ Grid*. Kurucz CD-ROM No. 13 (Cambridge, MA: Smithsonian Astrophysical Observatory), 13
- Lang, D., Hogg, D. W., Mierle, K., Blanton, M., & Roweis, S. 2010, *AJ*, 139, 1782
- Lidov, M. L. 1962, *P&SS*, 9, 719
- Lindgren, L., Hernández, J., Bombrun, A., et al. 2018a, *A&A*, 616, A2
- Lindgren, L., Hernández, J., Bombrun, A., et al. 2018b, *Gaia DR2 Astrometry* https://www.cosmos.esa.int/documents/29201/1770596/Lindgren_GaiaDR2_Astrometry_extended.pdf
- Madhusudhan, N., Crouzet, N., McCullough, P. R., Deming, D., & Hedges, C. 2014, *ApJL*, 791, L9
- Maxted, P. F. L., Anderson, D. R., Collier Cameron, A., et al. 2016, *A&A*, 591, A55
- McCullough, P. R., Burke, C. J., Valenti, J. A., et al. 2008, arXiv:0805.2921
- McCullough, P. R., Stys, J. E., Valenti, J. A., et al. 2005, *PASP*, 117, 783
- McCullough, P. R., Stys, J. E., Valenti, J. A., et al. 2006, *ApJ*, 648, 1228
- McCully, C., Volgenau, N. H., Harbeck, D.-R., et al. 2018, *Proc. SPIE*, 10707, 107070K
- McLaughlin, D. B. 1924, *ApJ*, 60, 22
- Ngo, H., Knutson, H. A., Hinkley, S., et al. 2015, *ApJ*, 800, 138
- Ngo, H., Knutson, H. A., Hinkley, S., et al. 2016, *ApJ*, 827, 8
- Nortmann, L., Pallé, E., Salz, M., et al. 2018, *Sci*, 362, 1388
- Paxton, B., Bildsten, L., Dotter, A., et al. 2011, *ApJS*, 192, 3
- Paxton, B., Cantiello, M., Arras, P., et al. 2013, *ApJS*, 208, 4
- Paxton, B., Marchant, P., Schwab, J., et al. 2015, *ApJS*, 220, 15
- Pepe, F., Mayor, M., Galland, F., et al. 2002, *A&A*, 388, 632
- Pepper, J., Pogge, R. W., DePoy, D. L., et al. 2007, *PASP*, 119, 923
- Perruchot, S., Kohler, D., Bouchy, F., et al. 2008, *Proc. SPIE*, 7014, 70140J
- Perryman, M., Hartman, J., Bakos, G. Á., & Lindgren, L. 2014, *ApJ*, 797, 14
- Pickles, A., & Depagne, É. 2010, *PASP*, 122, 1437
- Piskorz, D., Knutson, H. A., Ngo, H., et al. 2015, *ApJ*, 814, 148
- Pollacco, D. L., Skillen, I., Collier Cameron, A., et al. 2006, *PASP*, 118, 1407
- Ricker, G. R., Winn, J. N., Vanderspek, R., et al. 2015, *JATIS*, 1, 014003
- Rossiter, R. A. 1924, *ApJ*, 60, 15
- Santos, N. C., Sousa, S. G., Mortier, A., et al. 2013, *A&A*, 556, A150
- Sarkis, P., Henning, T., Hartman, J. D., et al. 2018, *AJ*, 156, 216
- Schlafly, E. F., & Finkbeiner, D. P. 2011, *ApJ*, 737, 103
- Schlaufman, K. C. 2010, *ApJ*, 719, 602
- Sheets, H. A., & Deming, D. 2017, *AJ*, 154, 160
- Sing, D. K., Fortney, J. J., Nikolov, N., et al. 2016, *Natur*, 529, 59
- Skrutskie, M. F., Cutri, R. M., Stiening, R., et al. 2006, *AJ*, 131, 1163
- Snedden, C. A. 1973, PhD thesis, The Univ. of Texas at Austin
- Sousa, S. G., Santos, N. C., Mayor, M., et al. 2008, *A&A*, 487, 373
- Southworth, J. 2015, *JKTLD: Limb Darkening Coefficients, Astrophysics Source Code Library*, ascl:1511.016
- Stassun, K. G., & Torres, G. 2018, *ApJ*, 862, 61
- Steffen, J. H., Ragozzine, D., Fabrycky, D. C., et al. 2012, *PNAS*, 109, 7982
- Sullivan, P. W., Winn, J. N., Berta-Thompson, Z. K., et al. 2015, *ApJ*, 809, 77
- Sullivan, P. W., Winn, J. N., Berta-Thompson, Z. K., et al. 2017, *ApJ*, 837, 99
- Tamuz, O., Mazeh, T., & Zucker, S. 2005, *MNRAS*, 356, 1466
- Torres, G., Andersen, J., & Giménez, A. 2010, *A&ARv*, 18, 67
- Winn, J. N., Fabrycky, D., Albrecht, S., & Johnson, J. A. 2010a, *ApJL*, 718, L145
- Winn, J. N., & Fabrycky, D. C. 2015, *ARA&A*, 53, 409
- Winn, J. N., Johnson, J. A., Howard, A. W., et al. 2010b, *ApJ*, 718, 575
- Wright, C. O., Egan, M. P., Kraemer, K. E., & Price, S. D. 2003, *AJ*, 125, 359